Solar Energy 144 (2017) 569–579

Contents lists available at ScienceDirect

Solar Energy

journal homepage: www.elsevier.com/locate/solener

# A generic solar-thermochemical reactor model with internal heat diffusion for counter-flow solid heat exchange

Christoph P. Falter [a,*], Robert Pitz-Paal [b]

[a] Bauhaus Luftfahrt, Willy-Messerschmitt-Straße 1, 82024 Taufkirchen, Germany
[b] DLR, Institute of Solar Research, Linder Höhe, 51147 Köln, Germany

ARTICLE INFO

Article history:
Received 18 October 2016
Received in revised form 25 January 2017
Accepted 28 January 2017

Keywords:
Solar fuel
Redox cycle
Heat recovery
Model

ABSTRACT

For nonstoichiometric redox reactions that produce CO and $H_2$ from $CO_2$ and $H_2O$, heat recuperation from the solid phase is a promising mechanism to improve the cycle efficiency. Many different approaches to heat recuperation and gas separation have been presented in solar thermochemical reactor concepts recently. To describe the many possible degrees of freedom in the reactor design, a generic reactor model is described for two-step redox reactions of solid pieces of reactant moving in counter flow between reduction and oxidation chambers. The reactive material is assumed to be porous ceria, where heat recuperation from the solid phase is achieved through radiation heat exchange between reduced and oxidized elements moving in opposite directions. A separation wall prevents gas cross-over and provides structural support. Heat transfer by radiation in the porous material is modeled with the Rosseland diffusion approximation and by conduction with the three resistor model. The model can be adapted to a wide range of reactor concepts.

A study of crucial design parameters shows that heat diffusion in the reactive material can have a significant influence on the performance of the heat exchanger. If the time required for heat diffusion is large with respect to the total residence time in the heat exchanger, the material thickness can be decreased to enhance the share of the material actively participating in the heat exchange process. Furthermore, at the relevant temperatures, radiation dominates the heat exchange within the porous structure, thus the overall heat exchange can be enhanced through an increase of porosity. Heat exchanger length and residence time are correlated, allowing different combinations of these two variables at constant heat exchanger efficiency. In general, efficiencies close to 70% are possible with an adequate parameter combination. However, the achievement of the maximum heat exchanger efficiency requires a minimum number of chambers and thus physical length, as irreversibilities are reduced for a larger number of intermediate temperature levels.

The presented generic model includes the description of heat diffusion within the reactive material, is a valuable tool for the design of heat exchangers, and can be used to identify technically interesting reactor concepts for the achievement of high energy conversion efficiencies.

## 1. Introduction

The transition of the energy basis from conventional sources such as coal, natural gas, and crude oil, to renewable sources is a major challenge that involves large investments and the development of new energy technologies. In case of the generation of electrical energy, a significant increase in renewable generation capacity has been achieved in the past years reaching a share of 22% of the total electricity generation (International Energy Agency, 2016). In the transportation sector, however, the penetration with renewables has been considerably lower, owing to the fact that conventional fuels such as gasoline, diesel and jet fuel are ideally suited for the use in mobile applications. Their high energy and power density are requirements for the use in aviation, sea traffic and heavy-duty road transportation, while for light-duty road transportation, an electrification using batteries and electric motors is easier to implement and has seen a rising share in recent years. Given a rising demand at limited resources and concerns about climate change, the aim of a reliable and affordable energy source for transportation requires solutions such as the production of an energy-dense fuel based on renewable energy.

---

* Corresponding author.
E-mail addresses: christoph.falter@bauhaus-luftfahrt.net (C.P. Falter), robert.pitz-paal@dlr.de (R. Pitz-Paal).

http://dx.doi.org/10.1016/j.solener.2017.01.063
0038-092X/

## Nomenclature

| | |
|---|---|
| $A$ | area [$m^2$] |
| $A_{he,ext}$ | external area of heat exchanger chamber facing the environment [$m^2$] |
| $C$ | concentration ratio of solar radiation [–] |
| $c_{p,CeO_2}$ | heat capacity of ceria at constant pressure [$J\ mol^{-1}\ K^{-1}$] |
| $c_{p,CO}$ | heat capacity of CO at constant pressure [$J\ mol^{-1}\ K^{-1}$] |
| $c_{p,CO_2}$ | heat capacity of $CO_2$ at constant pressure [$J\ mol^{-1}\ K^{-1}$] |
| $c_{p,O_2}$ | heat capacity of $O_2$ at constant pressure [$J\ mol^{-1}\ K^{-1}$] |
| $d_{mean}$ | mean diameter [m] |
| $g_0$ | parameter used in the three resistor model [–] |
| $g_1$ | parameter used in the three resistor model [–] |
| $\Delta H_{red}$ | reduction enthalpy [$J\ mol^{-1}$] |
| $I$ | intensity of solar radiation [$W\ m^{-2}$] |
| $k_f$ | thermal conductivity of fluid phase [$W\ m^{-1}\ K^{-1}$] |
| $k_s$ | thermal conductivity of solid phase [$W\ m^{-1}\ K^{-1}$] |
| $m$ | number of computational layers in element of reactive material [–] |
| $N$ | number of calculations [–] |
| $\dot{n}_{CeO_2}$ | molar flow rate of ceria [$mol\ s^{-1}$] |
| $\dot{n}_{CO}$ | molar flow rate of CO [$mol\ s^{-1}$] |
| $\dot{n}_{CO_2}$ | molar flow rate of $CO_2$ [$mol\ s^{-1}$] |
| $\dot{n}_{O_2}$ | molar flow rate of oxygen [$mol\ s^{-1}$] |
| $p_{O_2}$ | oxygen partial pressure relative to standard state [–] |
| $P_{aux}$ | auxiliary electrical power needed to operate reactor [W] |
| $P_{pump}$ | electrical power required for operation of vacuum pump [W] |
| $P_{sep,CO/CO_2}$ | electrical power required for gas separation of $CO/CO_2$-mixture [W] |
| $\dot{Q}_{aux}$ | solar power needed for auxiliary processes [W] |
| $\dot{Q}_{heat,CeO_2}$ | solar power needed to heat ceria [W] |
| $\dot{Q}_{heat,CO_2}$ | solar power needed to heat $CO_2$ [W] |
| $\dot{Q}_{heatexchange}$ | net rate of energy transferred between ceria elements in upper chamber half and lower chamber half of heat exchanger [W] |
| $\dot{Q}_{loss,conv}$ | thermal power lost by convection from heat exchanger chamber half [W] |
| $\dot{Q}_{loss,rad}$ | thermal power lost by radiation from heat exchanger chamber half [W] |
| $\dot{Q}_{products}$ | thermal power recovered from gaseous products [W] |
| $\dot{q}_{rad}$ | radiative heat flux [$W\ m^{-2}$] |
| $\dot{Q}_{red,CeO_2}$ | solar power needed to reduce ceria [W] |
| $\dot{Q}_{rerad}$ | rate of radiation heat losses from the reduction chamber [W] |
| $\dot{Q}_{solar}$ | solar power input to reactor [W] |
| $\mathcal{R}$ | ideal gas constant [$J\ mol^{-1}\ K^{-1}$] |
| $s$ | sample standard deviation [–] |
| $\Delta t$ | residence time in heat exchanger chamber [s] |
| $t_{CI,\nu}$ | t-value of the student t function for the confidence interval CI and $\nu = N - 1$ degrees of freedom |
| $T$ | temperature [K] |
| $T_0$ | ambient temperature [K] |
| $T_H$ | reduction temperature [K] |
| $T_{he,end,j}$ | temperature of $j$-th layer of reactive material at the end of the heat exchanger [K] |
| $\overline{T}_i$ | arithmetic mean temperature at position i |
| $T_L$ | oxidation temperature [K] |
| $T^n$ | temperature in time step $n$ [K] |
| $T^{n+1}$ | temperature in time step $n + 1$ [K] |
| $T_{pump}$ | temperature of vacuum pump [K] |
| $T_{RPC \rightarrow sw}$ | temperature of RPC in lower chamber half facing separating wall [K] |
| $T_{sw \rightarrow RPC}$ | temperature of separating wall facing RPC in lower chamber half [K] |
| $T_{wall}$ | temperature of heat exchanger wall facing surroundings [K] |

*Greek letters*

| | |
|---|---|
| $\alpha$ | absorption coefficient in Monte Carlo analysis [–] |
| $\alpha_{conv}$ | convective heat transfer coefficient at heat exchanger wall [$W\ m^{-1}\ K^{-1}$] |
| $\beta$ | extinction coefficient [$m^{-1}$] |
| $\beta_R$ | Rosseland mean attenuation coefficient [$m^{-1}$] |
| $\delta$ | oxygen nonstoichiometry of ceria [–] |
| $\delta_{ox}$ | oxygen nonstoichiometry of oxidized ceria [–] |
| $\delta_{red}$ | oxygen nonstoichiometry of reduced ceria [–] |
| $\varepsilon_{CeO_2}$ | emissivity of ceria [–] |
| $\varepsilon_{sw}$ | emissivity of separating wall [–] |
| $\varepsilon_{wall}$ | emissivity of heat exchanger wall facing the environment [–] |
| $\eta$ | efficiency (concentrated solar to chemical energy stored in CO) [–] |
| $\eta_{abs}$ | absorption efficiency of reactor [–] |
| $\eta_{gasrec}$ | recuperation efficiency of gases leaving the reduction and oxidation chambers [–] |
| $\eta_{he}$ | heat exchanger efficiency [–] |
| $\eta_{heat-to-electricity}$ | conversion efficiency of heat to electricity [–] |
| $\eta_{pump}$ | efficiency of vacuum pump [–] |
| $\lambda$ | thermal conductivity [$W\ m^{-1}\ K^{-1}$] |
| $\lambda_{rad}$ | radiative conductivity [$W\ m^{-1}\ K^{-1}$] |
| $\sigma$ | Stefan-Boltzmann constant [$W\ m^{-2}\ K^{-4}$] |
| $\varphi$ | porosity [–] |
| $\Psi_1$ | parameter used in the calculation of the extinction coefficient [–] |

Due to its abundance and global availability, solar energy is an attractive primary energy source for the production of liquid fuels. The solar thermochemical pathway uses concentrated solar energy to thermochemically split water and carbon dioxide into syngas and the Fischer-Tropsch process to synthesize liquid hydrocarbon fuels. It offers the potential of a low climate impact at a large energy conversion efficiency (Falter et al., 2016; Steinfeld and Epstein, 2001). For its implementation, different materials and processes have been suggested, where in recent years, non-volatile redox reactions with cerium oxide (ceria) have shown promising experimental results (Chueh et al., 2010; Furler et al., 2014, 2012a; Marxer et al., 2015). In most implementations, ceria is only partially reduced to retain the material in its solid fluorite structure and to thus enable a process without phase changes. This facilitates the reactor design considerably, as high temperature gas separations are avoided. However, the downside is that only a small fraction of the reactive material actually participates in the redox cycle, leading to a large thermal mass with respect to the produced amount of syngas. As the redox cycle is performed under a temperature swing, a relatively large amount of energy is required for the heating of the material to the reduction temperature. In theoretical analyses it was shown that for nonstoichiometric ceria cycles, energy recuperation from the temperature swing is imperative to achieve high levels of energy conversion efficiency (Falter et al., 2015; Lapp et al., 2012).

Different reactor concepts have been presented including heat recuperation from the solid and the gaseous phase, e.g. the CR5-reactor (Diver et al., 2008), where counter-rotating rings of reactive material are reduced by solar radiation on one side and oxidized on the opposite side, exchanging heat in between the reaction zones. Another similar concept is shown in Lapp et al. (2013), where an inert cylinder rotates in the opposite direction of the reactive cylinder surrounding it which is directly heated by solar radiation. In Ermanoski et al. (2013), a particle reactor concept is presented which includes heat exchange between the oxidized and reduced particles and an inherent gas separation through the packed bed of reduced particles. Direct heat exchange between reactive particles and heat exchanger particles is suggested in Felinks et al. (2014), indicating a high recuperation potential. Very different approaches exist for the implementation of heat recuperation from the solid phase of nonstoichiometric redox reactions. Efficiency analyses of solar thermochemical syngas production have followed either a fundamental thermodynamic path or have focused on the detailed analysis of a specific reactor concept. However, for the description of a large number of technically interesting implementations, a generic reactor model is required which was presented with an upper-bound performance estimation for idealized internal heat transfer within the reactive medium in Falter et al. (2015). It was noted that heat diffusion in the material may have a significant influence on the heat exchanger performance and should thus be analyzed in more detail. In this work, the presented model is used as a basis and further developed to include the modeling of heat transfer within the reactive medium to analyze its influence on the overall performance of heat exchanger concepts. A parameter study of fundamental variables then gives insight into the behavior of counter-flow heat exchangers operating with optically thick material to improve the energy conversion efficiency of solar thermochemical syngas production.

## 2. Model description and numerical solution algorithm

A generic and modular reactor concept for two-step thermochemical processes is described comprising a reduction chamber ($i = 1$), intermediate chambers for heat exchange ($i = 2\ldots n-1$) and an oxidation chamber ($i = n$, Fig. 1). Elements of reactive material are heated by concentrated solar radiation in the reduction chamber and reoxidized with an oxidant in the oxidation chamber, i.e. $CO_2$ or $H_2O$ or a mixture thereof, to produce syngas. In the following, without loss of generality, $CO_2$ is used as the oxidant. An excess amount of oxidant is supplied to the oxidation for thermodynamic and kinetic reasons and the resulting mixture of CO and $CO_2$ is separated to reduce the amount of $CO_2$ contamination for the Fischer-Tropsch reaction. A vacuum pump reduces the oxygen partial pressure in the reduction chamber and the $n$-1th chamber to prevent gases from crossing over from the oxidation chamber. The heat exchanger is thus kept at the pressure of the reduction chamber.

In between the reaction chambers, heat is exchanged by radiation between the reduced and oxidized elements moving in counter-flow through the heat exchanger chambers. A wall ensures separation of the gas atmospheres between chamber halves to prevent gas cross-over, where the wall is made from HfC/SiC having a high emissivity and thermal conductivity to promote the heat exchange between the elements (Fig. 2). As SiC may undergo a chemical reaction with ceria at elevated temperatures, the wall is further separated from the elements by a layer of non-porous $Al_2O_3$. A thickness of 1 mm is chosen for the separation walls and the fluid gap between separation wall and element in the lower chamber half.

Equilibrium thermodynamics together with initial species concentration and constant temperatures are used to calculate the amount of nonstoichiometry and syngas production in the reaction chambers. An energy balance of the heat exchanger including radiation heat exchange between the chamber halves and heat losses to the surroundings then gives the temperature distribution of the elements.

As a reactive material, a reticulated porous ceramic (RPC) made from ceria undergoing nonstoichiometric redox reactions, is assumed, as it has been shown to be a suitable material with promising efficiencies in experiments (Furler et al., 2014, 2012a; Marxer et al., 2015). The description of other materials is easily possible if the respective material properties are known. Reduction is performed at an elevated temperature $T_H$ and reduced oxygen partial pressure $p_{O_2}$. The oxygen nonstoichiometry increases from $\delta_{ox}$ after oxidation to $\delta_{red}$ after reduction, see Eq. (1).

$$\frac{1}{\delta_{red}-\delta_{ox}}CeO_{2-\delta_{ox}} \rightarrow \frac{1}{\delta_{red}-\delta_{ox}}CeO_{2-\delta_{red}} + \frac{1}{2}O_2 \tag{1}$$

$$\frac{1}{\delta_{red}-\delta_{ox}}CeO_{2-\delta_{red}} + H_2O \rightarrow \frac{1}{\delta_{red}-\delta_{ox}}CeO_{2-\delta_{ox}} + H_2 \tag{2}$$

$$\begin{array}{c} \underline{\dfrac{1}{\delta_{red}-\delta_{ox}}CeO_{2-\delta_{red}} + CO_2 \rightarrow \dfrac{1}{\delta_{red}-\delta_{ox}}CeO_{2-\delta_{ox}} + CO} \\ H_2O \rightarrow \dfrac{1}{2}O_2 + H_2 \\ CO_2 \rightarrow \dfrac{1}{2}O_2 + CO \end{array} \tag{3}$$

In Ermanoski et al. (2013), a function was fitted to the experimental data of oxygen nonstoichiometry in ceria by Panlener et al. (1975), which is used here as well. The calculation of oxygen nonstoichiometry is performed using mass conservation in a closed

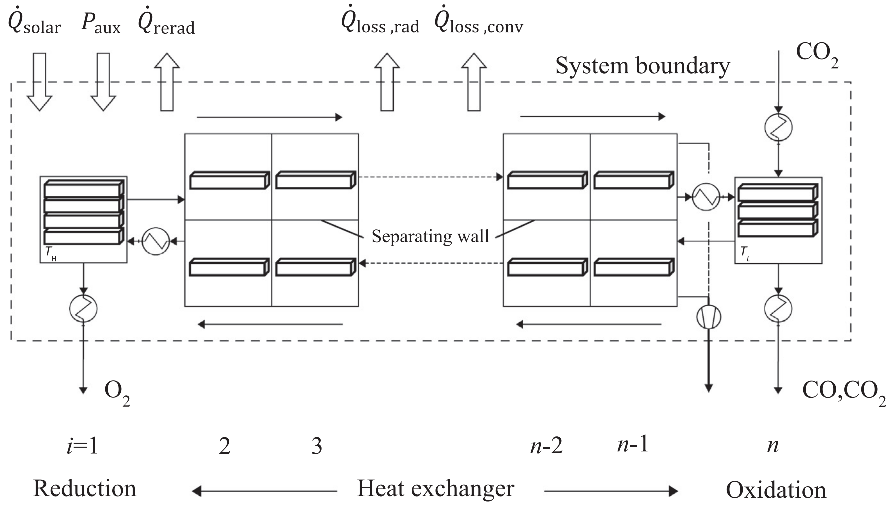

**Fig. 1.** Schematic of modular generic rector model including n chambers, one for reduction ($i = 1$) and oxidation ($i = n$), and $n$-2 heat exchanger chambers ($i = 2\ldots n-1$).

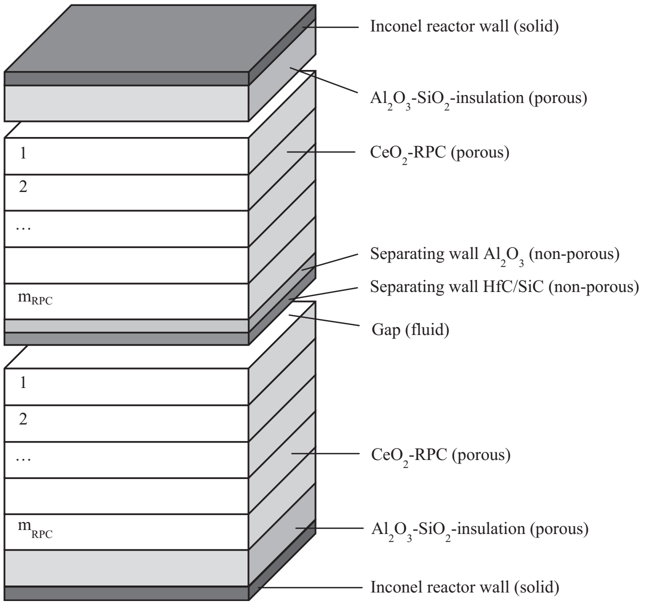

**Fig. 2.** Schematic of one representative heat exchanger chamber for the modeling of radiation heat exchange between chamber halves and internal heat transfer in the reactive medium and adjacent insulation.

system with defined initial gas concentrations and experimental data of enthalpy and entropy as a function of nonstoichiometry (Panlener et al., 1975), where the detailed derivation was shown in Falter et al. (2015).

### 2.1. Energy balance

The overall energy balance of the system is

$$\dot{Q}_{\mathrm{solar}} + P_{\mathrm{aux}} - \dot{Q}_{\mathrm{heat,CeO_2}} - \dot{Q}_{\mathrm{red,CeO_2}} - \dot{Q}_{\mathrm{heat,CO_2}} + \dot{Q}_{\mathrm{products}} - \dot{Q}_{\mathrm{rerad}} - P_{\mathrm{pump}} - P_{\mathrm{sep,\frac{CO}{CO_2}}} = 0, \tag{4}$$

where the solar power input to the reactor is

$$\dot{Q}_{\mathrm{solar}} = \frac{1}{\eta_{\mathrm{abs}}}\left(\dot{Q}_{\mathrm{heat,CeO_2}} + \dot{Q}_{\mathrm{red,CeO_2}} + \dot{Q}_{\mathrm{heat,CO_2}} - \dot{Q}_{\mathrm{products}}\right). \tag{5}$$

$\eta_{\mathrm{abs}}$ is the absorption efficiency of the solar reduction chamber and is, assuming a well-insulated blackbody cavity, $\eta_{\mathrm{abs}} = 1 - \frac{\sigma T^4}{I \cdot C}$, where $I$ is the intensity of solar radiation and $C$ the concentration efficiency which are assumed to be 1 kW m$^{-2}$ and 3000 suns, respectively.

$\dot{Q}_{\mathrm{heat,CeO_2}}$ is the solar power required to raise the temperature of the oxidized ceria element to the reduction temperature $T_{\mathrm{H}}$,

$$\dot{Q}_{\mathrm{heat,CeO_2}} = (1-\eta_{\mathrm{he}})\dot{n}_{\mathrm{CeO_2}} \int_{T_{\mathrm{L}}}^{T_{\mathrm{H}}} c_{p,\mathrm{CeO_2}}(T)\mathrm{d}T = \dot{n}_{\mathrm{CeO_2}} \int_{T_{\mathrm{he,end},j}}^{T_{\mathrm{H}}} c_{p,\mathrm{CeO_2}}(T)\mathrm{d}T, \tag{6}$$

where the heat exchanger efficiency $\eta_{\mathrm{he}}$ is defined as

$$\eta_{\mathrm{he}} = \frac{\sum_1^m \int_{T_{\mathrm{L}}}^{T_{\mathrm{he,end,j}}} c_{p,\mathrm{CeO_2}}(T)dT}{m\int_{T_{\mathrm{L}}}^{T_{\mathrm{H}}} c_{p,\mathrm{CeO_2}}(T)dT}, \tag{7}$$

and $T_{\mathrm{he,end},j}$ is the temperature of the $j$-th layer of the ceria element at the end of the heat exchanger before entering the reduction chamber (Fig. 2).

$\dot{Q}_{\mathrm{red,CeO_2}}$ is the rate of energy required to reduce the material from $\delta_{\mathrm{ox}}$ to $\delta_{\mathrm{red}}$

$$\dot{Q}_{\mathrm{red,CeO_2}} = \dot{n}_{\mathrm{CeO_2}}\Delta H_{\mathrm{red}} = \dot{n}_{\mathrm{CeO_2}} \int_{\delta_{\mathrm{ox}}}^{\delta_{\mathrm{red}}} \Delta H_{\mathrm{CeO_2}}(\delta)\mathrm{d}\delta. \tag{8}$$

$\dot{Q}_{\mathrm{heat,CO_2}}$ is the thermal power required to heat CO$_2$ from ambient temperature to the oxidation temperature

$$\dot{Q}_{\mathrm{heat,CO_2}} = \dot{n}_{\mathrm{CO_2}} \int_{T_0}^{T_{\mathrm{L}}} c_{p,\mathrm{CO_2}}(T)\mathrm{d}T. \tag{9}$$

The properties of CO$_2$ and all other gases are calculated with tables from Engineering Toolbox (2015) and Kleiber and Joh (2013).

$\dot{Q}_{\mathrm{products}}$ is the thermal power which is recovered from gases leaving the reduction and oxidation reactions (O$_2$, CO, CO$_2$) with an efficiency of $\eta_{\mathrm{gasrec}}$.

$$\dot{Q}_{\mathrm{Products}} = \eta_{\mathrm{gasrec}}\left(\dot{n}_{\mathrm{CO}} \int_{T_0}^{T_{\mathrm{L}}} c_{p,\mathrm{CO}}(T)\mathrm{d}T + \dot{n}_{\mathrm{CO_2}} \int_{T_0}^{T_{\mathrm{L}}} c_{p,\mathrm{CO_2}}(T)\mathrm{d}T + \dot{n}_{\mathrm{O_2}} \int_{T_0}^{T_{\mathrm{L}}} c_{p,\mathrm{O_2}}(T)\mathrm{d}T\right). \tag{10}$$

Mechanical energy which is required to move ceria is neglected, as it is small compared to the heating value of the produced syngas. Liberated energy in the exothermic oxidation reaction is assumed to maintain the ceria temperature in the oxidation chamber and otherwise to be lost.

The vacuum pump power is

$$P_{\mathrm{pump}} = \frac{\dot{n}_{\mathrm{O_2}} \mathscr{R} T_{\mathrm{pump}} \ln(p_{\mathrm{O_2}}^{-1})}{\eta_{\mathrm{pump}}}, \tag{11}$$

where the vacuum pump efficiency $\eta_{\mathrm{pump}}$ is fitted to experimental data provided by a manufacturer (Felinks, 2014; Pfeiffer Vacuum, 2014) and is $\eta_{\mathrm{pump}} = 0.8437 p_{\mathrm{O_2}}^{0.3662}$, where the released oxygen in the reduction chamber and the oxidant lost through the periodic opening of the oxidation chamber is removed. The oxygen flow rate $\dot{n}_{\mathrm{O_2}}$ is derived from the stoichiometry of the overall reaction as half of the carbon monoxide flow rate, the pump temperature $T_{\mathrm{pump}}$ is assumed to be the ambient temperature and $p_{\mathrm{O_2}}$ is the partial pressure of oxygen during reduction.

The CO/CO$_2$ separation is assumed to be complete, i.e. pure streams of CO and CO$_2$ are produced. Literature data for the CO$_2$ capture from a flue gas stream of a fossil power plant are chosen as a reference (Zeman, 2007), where 132 kJ of heat and 9 kJ of electricity are required for the capture of one mol of CO$_2$. The auxiliary electrical power input $P_{\mathrm{aux}} = P_{\mathrm{pump}} + P_{\mathrm{sep,CO/CO_2}}$ is then divided by the conversion efficiency of heat to electricity $\eta_{\mathrm{heat\text{-}to\text{-}electricity}}$ to arrive at the auxiliary thermal power input $\dot{Q}_{\mathrm{aux}} = \frac{P_{\mathrm{aux}}}{\eta_{\mathrm{heat\text{-}to\text{-}electricity}}}$.

The efficiency of the reactor is defined as

$$\eta = \frac{\text{chemical energy stored in product}}{\text{solar power in to reactor} + \text{auxiliary power}} = \frac{\dot{n}_{\mathrm{CO}}\mathrm{HHV}_{\mathrm{CO}}}{\dot{Q}_{\mathrm{solar}} + \dot{Q}_{\mathrm{aux}}}. \tag{12}$$

This definition accounts the energy input at the system boundary of the reactor, i.e. the concentration efficiency and the primary energy conversion efficiency for the heat used for the auxiliary power can be included depending on the chosen technologies.

The temperature of the elements in the heat exchanger is calculated with an energy balance of the single chambers (exemplary chamber shown in Fig. 2), where each chamber is subdivided into upper and lower chamber half. The domains of insulation and reactive materials are discretized with the finite volume method. Heat is transferred by radiation between the separating wall and the element in the lower chamber half, by conduction in the separating wall and the reactor wall, by conduction and radiation in the elements and in the porous insulation, and heat is lost to the environment through convection and radiation.

The radiation heat transfer between the separating wall and the lower chamber half is modeled with the expression for infinite parallel flat plates (Howell et al., 2011)

$$\dot{Q}_{\text{heat exchange}} = \frac{A\sigma\left(T^4_{\text{sw}\to\text{RPC}} - T^4_{\text{RPC}\to\text{sw}}\right)}{\frac{1}{\varepsilon_{\text{sw}}} + \frac{1}{\varepsilon_{\text{CeO}_2}} - 1}, \tag{13}$$

where $A$ is the active area of heat exchange, $\sigma$ is the Stephan-Boltzmann constant, $T_{\text{sw}\to\text{RPC}}$ and $T_{\text{RPC}\to\text{sw}}$ are the temperatures of the separating wall facing the lower chamber half and of the RPC facing the separating wall, respectively. The emissivity of the wall is 0.85 (Ultramet, 2015) and that of ceria $\varepsilon_{\text{CeO}_2}$ is a function of temperature, which is taken from Touloukian et al. (1971). The high temperatures in the heat exchanger cause a temperature increase of the outside wall above the temperature of the surroundings and heat is lost by radiation and convection.

Radiation heat transfer from the reactor wall to the environment is

$$\dot{Q}_{\text{loss,rad}} = \varepsilon_{\text{wall}} A_{\text{he,ext}} \sigma \left(T^4_{\text{wall}} - T^4_0\right), \tag{14}$$

and by convection

$$\dot{Q}_{\text{loss,conv}} = \alpha_{\text{conv}} A_{\text{he,ext}} \Delta T = \alpha A_{\text{he,ext}} (T_{\text{wall}} - T_0), \tag{15}$$

where the convective heat transfer coefficient $\alpha_{\text{conv}}$ is conservatively assumed to be 15 $\text{W m}^{-2}\,\text{K}^{-1}$ (Hischier et al., 2009) and the area facing the environment is defined to be six times the active area of heat exchange, as is the case for example for cubic elements $A_{\text{he,ext}} = 6 \cdot A$.

The temperature distribution in the heat exchanger is then derived by pseudo-transient continuation starting from a first guess (a predefined temperature distribution which depends on heat exchanger length and temperature levels, which in general increases in temperature from the heat exchanger outside to its inside and from the oxidation to the reduction chamber) until a steady state is reached, i.e. until the maximum temperature change of the elements of two consecutive time steps is smaller than a defined value $\left|\frac{T^{n+1} - T^n}{T^{n+1}}\right| \leqslant 10^{-4}$.

### 2.2. Calculation of radiation and conduction in porous domains

The radiation source term is modeled with the Rosseland diffusion approximation assuming an absorbing, emitting, and isotropically scattering optically thick medium (Howell et al., 2011).

$$\nabla \dot{q}_{\text{rad}} = -\nabla(\lambda_{\text{rad}} \nabla T), \tag{16}$$

where the thermal radiative conductivity $\lambda_{\text{rad}}$ for a refractive index of one is given by

$$\lambda_{\text{rad}} = \frac{16\sigma T^3}{3\beta_{\text{R}}}, \tag{17}$$

and where $\beta_{\text{R}}$ is the Rosseland mean attenuation coefficient and $\sigma$ is the Stefan-Boltzmann constant.

*RPC:* For the description of radiative heat transfer in reticulated porous ceramics, numerical solutions were obtained for tomographic scans of material and compared with models from the literature in Suter et al. (2014). The model using multi-faced particles after Loretz et al. (2008) was found to reproduce the numerical solution best and is used here in the following. The medium is further assumed to be gray, making $\beta_{\text{R}}$ equal to the extinction coefficient $\beta$ which is defined by Loretz et al. as a function of porosity

$$\beta = \Psi_1 \cdot \frac{\sqrt{1-\varphi}}{d_{\text{mean}}}, \tag{18}$$

$$d_{\text{mean}} = 2.20 \times 10^{-3} \cdot \varphi + 4.59 \times 10^{-4}\ \text{m} \tag{19}$$

with the fitting parameter $\Psi_1 = 1.765$ and the mean pore diameter $d_{\text{mean}}$. The pore diameter is a function of porosity $\varphi$, i.e. an increase in porosity is directly linked to an increase in pore diameter and both variables cannot be chosen independently.

Conduction through the porous medium is described with the three-resistor model which uses a linear combination of the minimum possible conductivity in the serial arrangement of phases and of the maximum possible conductivity in the parallel arrangement of the phases to derive the overall thermal conductivity of the porous medium (Suter et al., 2014).

$$\lambda = \left(1 - \sqrt{g_0 - g_1\varphi}\right) \frac{k_{\text{f}}}{\varphi + (1-\varphi)\frac{k_{\text{f}}}{k_{\text{s}}}} + \sqrt{g_0 - g_1\varphi}\left(\varphi k_{\text{f}} + (1-\varphi)k_{\text{s}}\right) \tag{20}$$

The values of the parameters $g_0$ and $g_1$ are 0.754 and 0.829 (Suter et al., 2014), $k_{\text{f}}$ and $k_{\text{s}}$ are the thermal conductivities of the fluid and solid material, and $\varphi$ is the porosity of the porous domain. The effective thermal conductivity of the porous medium $\lambda$ is then used in the energy conservation equation.

*Insulation:* The modeled porous insulation is comprised of fibers of $Al_2O_3$ and $SiO_2$. As the pore mean diameter is not known, experimental values for the Rosseland mean attenuation coefficient and for the thermal conductivity are used to describe the thermal energy transfer across the insulation. The former are taken from Zhang et al. (2007) and the latter from the manufacturer of the type M-35 buster insulation (Zircar Zirconia, 2015) which has also been used in solar thermochemical experiments (Chueh and Haile, 2010; Furler et al., 2014, 2012b; Marxer et al., 2015).

### 2.3. Material properties

In the following, the data sources for the properties of materials used in the model are shown and assumptions are described. The convective heat transfer coefficient from the reactor wall to the surroundings at 300 K is assumed to be 15 $\text{W m}^{-1}\,\text{K}^{-1}$ (Hischier et al., 2009). Table 3 in the annex gives an overview of the material properties.

## 3. Model validation

The overall heat exchange of reactive material in counter-flow is comprised of a succession of identical heat exchange processes of RPCs at different temperatures in the single chambers of the heat exchanger. In order to validate the model, the following test case representing only one chamber is used as an assessment for the overall process. The single chamber heat exchange between two porous ceramics separated by a thin wall is solved with the proposed reactor model and with a Monte Carlo simulation, where the result of the latter is taken as a reference.

For the test case, defined initial temperatures are chosen for the RPCs and the adjacent separating wall which is made of two 1 mm-layers of $Al_2O_3$ and SiC/HfC, respectively. The former is used for the physical separation of SiC and $CeO_2$ which may undergo carbothermal reduction when brought into contact at high temperatures. The latter is a material used for protective coatings with a high emissivity, thermal conductivity and maximum operating temperature of over 2000 K (Ultramet, 2015). Material properties and boundary conditions of the calculation are shown in Fig. 3a and Table 1. In the Monte Carlo analysis, the resulting radiation heat term is inserted into the energy conservation equation which is then solved to obtain the temperature profile in the computational domain. Scattering is assumed to be isotropic and is described by the scattering coefficient $\sigma = \rho_{\text{s}} \cdot \beta$, where $\rho_{\text{s}}$ is the surface reflectance of partially reduced ceria, weighted by the black-body thermal emission, and $\beta$ is the extinction coefficient, both functions of temperature. The absorption coefficient $\alpha$ is then $\alpha = (1 - \rho_{\text{s}}) \cdot \beta$ (Furler, 2014). Heat conduction is modeled in both models with the three resistor model, so that the difference between the models is derived from the description of the radiative source term.

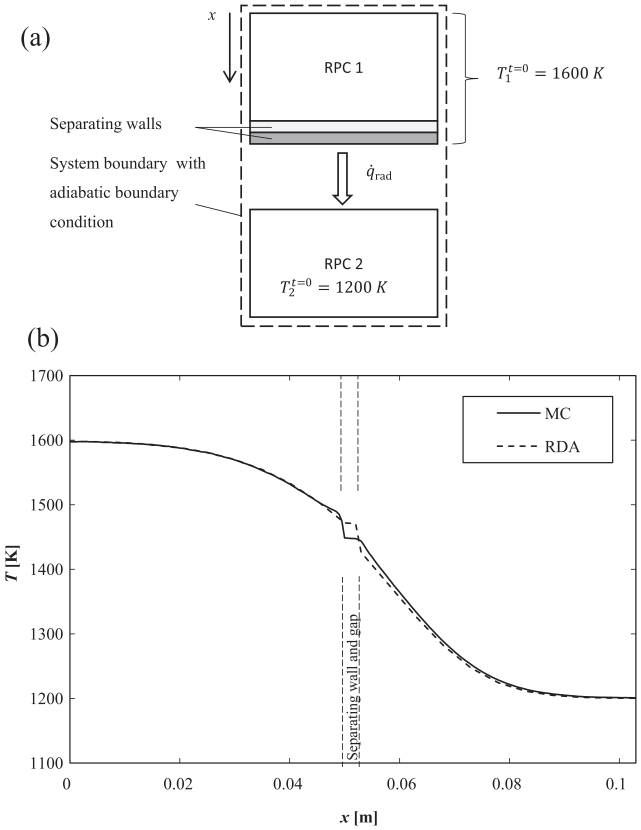

**Fig. 3.** (a) Schematic of test case used for validation of the Rosseland diffusion model with the Monte Carlo model. At the beginning of the simulation, two porous ceramics, separated by a layer of SiC/HfC and $Al_2O_3$ (1 mm thickness each) are at temperatures of 1600 K and 1200 K, respectively, with adiabatic boundary conditions towards the environment. In the transient simulation, the temperature profile of the RPCs and the separating walls is calculated after 40 s with both models and compared. (b) Temperature profiles obtained with the Monte Carlo model (MC) and the Rosseland diffusion approximation (RDA) for two RPCs (reticulated porous ceramic) separated by a layer of SiC/HfC and $Al_2O_3$ (1 mm thickness each), after 40 s of heat exchange. The starting temperatures are 1600 K for RPC 1 ($0 \leqslant x \leqslant 50$ mm) and the walls ($50 < x \leqslant 52$ mm), and 1200 K for RPC 2 ($53 \leqslant x \leqslant 103$ mm). The agreement between the models is very good except at the solid-fluid boundary, where the temperature is overpredicted by 1.6% by the RDA because of the anisotropy of radiation.

The equation solved in the first layer of the lower RPC is the following.

$$\frac{\sigma(T_{sw}^4 - T_k^4)}{\frac{1}{\varepsilon_{sw}}+\frac{1}{\varepsilon_{RPC}}-1} + \frac{\lambda_f(T_f - T_k)}{\Delta x_{gap}} - \frac{\lambda_{RPC}(T_k - T_{k+1})}{\Delta x_{RPC}} + \dot{Q}_{rad} = \frac{\rho \Delta x c_{p,RPC}\left(T_k^{m+1} - T_k^m\right)}{\Delta t} \qquad (21)$$

**Table 2**
Parameter values for example system.

| Parameter | Label | Value | Unit |
|---|---|---|---|
| Concentration ratio | $C$ | 3000 | – |
| Oxidation temperature | $T_L$ | 1000 | K |
| Reduction temperature | $T_H$ | 1800 | K |
| Temperature of surroundings | $T_0$ | 300 | K |
| Reduction pressure (relative to standard state of 1 atm) | $p_{red}$ | $10^{-3}$ | – |
| Oxidation pressure (relative to standard state of 1 atm) | $p_{ox}$ | 1.0 | atm |
| $CO_2$-flow (times min = $\delta_{red}$) in oxidation chamber | $f_{CO_2}$ | 2.0 | – |
| Number of chambers (including reaction chambers) | $n$ | 10 | – |
| Residence time in heat exchanger | $\Delta t$ | 40 | s |
| Mass of ceria piece | $m$ | 0.77 | kg |
| Porosity of reactive material | $\varphi$ | 0.8 | – |
| Efficiency of gas heat recovery | $\eta_{gasrec}$ | 0.5 | – |
| Conversion efficiency of heat to electricity | $\eta_{heat\text{-}to\text{-}electricity}$ | 0.4 | – |
| Convective heat transfer coefficient | $\alpha_{conv}$ | 15 | W m$^{-2}$ K$^{-1}$ |

$\lambda$ is thermal conductivity, $\Delta x$ is the thickness of the first layer of the RPC, $\Delta x_{gap}$ is the thickness of the gap, $\Delta t$ is the time step, and the subscripts “sw”, “f” and “k” denote the separation wall, fluid in the gap (assumed to be oxygen) and the first layer of the RPC. The superscript “m” refers to the time step. The radiation source term $\dot{Q}_{rad}$ appears only in the MC model and $\lambda_{RPC}$ is only the thermal conductivity in case of MC but the combined thermal and radiative conductivity in case of RDA.

The MC model is a statistical tool and uses random numbers to describe the radiation emitted in the computational domains. In order to reduce the variability of the results, the MC model is run ten times and the results are averaged and compared with the RDA solution. 95%-confidence intervals are calculated from the MC data using the *student t function*. All confidence intervals for the temperatures are below 1 K for a resolution of 100 layers per RPC.

In Fig. 3b), the temperature profiles for the test case are shown after 40 s of heat exchange, calculated with the Monte Carlo method for the radiation source term using 100 layers per RPC and the Rosseland diffusion approximation using 10 layers per RPC. The results of both models agree very well with an average deviation of 0.4%. The largest difference of 1.6% between the models is seen at the separating wall because the RDA can give erroneous results at boundaries where the radiation is anisotropic.

## 4. Parameter study

In the following, a parameter study of the thickness of the porous ceramic elements, their porosity and of the residence time and length of the heat exchanger is shown.

**Table 1**
Material properties and boundary conditions of Monte Carlo analysis for model validation.

| Variable | Value | Unit | Source |
|---|---|---|---|
| $T^{t=0}$ (upper RPC, sep. wall) | 1600 | K | – |
| $T^{t=0}$ (lower RPC) | 1200 | K | – |
| $\varepsilon_{Al_2O_3}$ | 0.4 | – | Touloukian and DeWitt (1972) |
| $\lambda_{Al_2O_3}$ | 35 | W m$^{-1}$ K$^{-1}$ | Accuratus (2016) |
| $\varepsilon_{SiC/HfC}$ | 0.85 | – | Ultramet (2015) |
| $\lambda_{SiC/HfC}$ | 80 | W m$^{-1}$ K$^{-1}$ | Ultramet (2015) |
| Simulation time | 40 | s | – |
| Number of rays | $2 \times 10^5$ | – | – |
| Time step | 0.01 | s | – |
| Extinction coefficient $\beta$ | $\frac{1.77\cdot\sqrt{1-\varphi}}{2.2\times10^{-3}\varphi+7.59\times10^{-4}}$ | m$^{-1}$ | |
| Scattering coefficient $\sigma$ | $(-6 \times 10^{-5} + 0.411)\beta$ | m$^{-1}$ | Furler (2014) |
| Absorption coefficient $\alpha$ | $(1 - (-6 \times 10^{-5} + 0.411))\beta$ | m$^{-1}$ | Furler (2014) |

### 4.1. Thickness of elements

The thickness of the elements of reactive material is varied to find its influence on heat exchanger efficiency and cycle efficiency. Overall heat transfer between the reduced and oxidized elements is composed of (i) radiation heat exchange between the top layer of the material in the lower chamber half and the separating wall, and (ii) the internal heat transfer within the reactive materials, as well as heat losses to the surroundings. The former (i) is limited by the emissivities of the materials and their temperatures, while the latter (ii) is limited by the effective thermal conductivity of the material which is determined by the porosity of the material, the thermal conductivities of the solid and fluid, and the radiative properties of the porous material. An increase of material thickness does not change the effective thermal conductivity (according to Eqs. (18) and (20)), however, it increases the mass and the distance for thermal transport in the material and therefore leads to a larger temperature drop in the element. With increasing thickness of the elements and at otherwise constant heat exchanger length and residence time, it is therefore expected that the temperature drop in the material will increase, not allowing all of the material to participate to the same degree in the heat exchange process. In Fig. 4, the efficiency of the heat exchanger $\eta_{\mathrm{he}}$ as defined in Eq. (7) and the cycle efficiency $\eta$ as defined by Eq. (12) is shown as a function of the material thickness which is varied between 0.02 m and 0.10 m at a porosity of 80% in a heat exchanger with 8 chambers at a residence time of 40 s. In general, the cycle efficiency $\eta$ does not vary significantly due to the comparably low efficiency level at the chosen operating point which is limited especially by the reduction temperature and pressure. Heat exchanger efficiency increases strongly for a decreasing material thickness: at 0.10 m $\eta_{\mathrm{he}} = 22.1\%$ and at 0.02 m thickness $\eta_{\mathrm{he}} = 71.0\%$. This significant improvement is due to the fact that at a defined heat exchanger length and specific residence time of the elements, there is a finite time for the thermal energy to be diffused in the material. Thinner elements have a lower mass and can be heated more quickly, while for larger thicknesses, parts of the material are participating poorly or not at all in the heat exchange between hot and cold elements which decreases heat exchanger efficiency.

In Fig. 5, the temperature profiles of the heat exchanger are shown for a material thickness of 0.02 m and 0.10 m. The heat exchanger has eight chambers, the temperatures of the reduction and oxidation chambers adjacent to the heat exchanger are 1800 K and 1000 K, respectively, and the residence time per chamber is 40 s. The temperature profiles thus show the temperature changes of the reactive material inside of the heat exchanger (compare also Fig. 1 for a general overview of the heat exchanger). Following the path of the colder elements ($i = 9 \rightarrow i = 2$), the heating process can be seen, where the final temperature in the heat exchanger is reached at $i = 2$. Comparing the final temperature of the two elements in (a) and (b) shows that the thinner material gets heated to temperatures above 1500 K with a maximum temperature difference of about 90 K (maximum temperature: 1630 K, minimum temperature: 1538 K). The thicker material on the other hand shows a much larger maximum temperature difference of over 600 K (maximum temperature: 1610 K, minimum temperature: 990 K) since the heat diffusion process within the material is slower than the heat exchange process between the chambers with the assumed residence time. Thus, for the larger material thickness and a total residence time of $8 \times 40\,\mathrm{s} = 320\,\mathrm{s}$, the internal heat diffusion process is limiting the heat exchange between hot and cold elements. Either a longer total residence time (through an increase of the residence time per chamber or an increase of the heat exchanger length) or a lower material thickness has thus to be chosen to increase the efficiency of the heat exchanger. The heating process thus becomes more efficient with a reduction of material thickness as already seen in Fig. 4. The influence of material thickness on heat exchanger efficiency is of course dependent on the specific properties of the heat exchanger which were fixed here in the operating point of the baseline case (Table 1). For a different number of heat exchanger chambers and residence times, the efficiency curve is shifted, however, the general functional dependency between material thickness and efficiency remains the same, as it is defined by the relative magnitude of heat transfer between the chamber halves and within the materials.

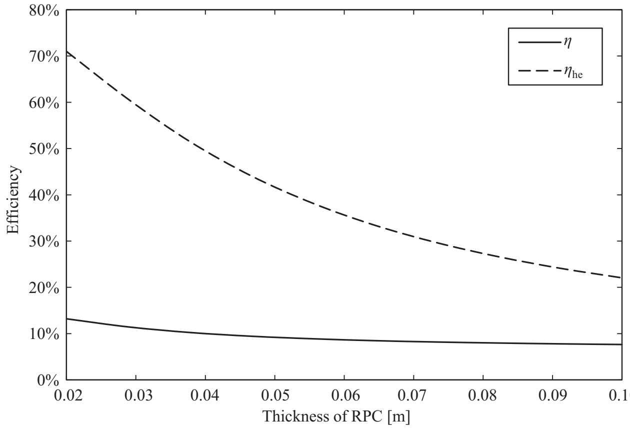

**Fig. 4.** Heat exchanger efficiency $\eta_{\mathrm{he}}$ and cycle efficiency $\eta$ as a function of RPC thickness. The heat exchanger has eight chambers, the residence time is 40 s and the porosity of the elements is 80%. Parameter values are shown in Table 2.

The supposition of facilitated heat transfer in elements with a lower thickness is therefore confirmed which leads to a first recommendation for the design of heat exchangers, i.e. the consideration of both heat exchange processes (i) between hot and cold material and (ii) within the materials itself.

### 4.2. Porosity of elements

A change in porosity both influences radiation heat exchange through the extinction coefficient (Eq. (18)) and conduction heat exchange through the effective thermal conductivity (Eq. (20)). An increase in porosity therefore enhances radiation heat exchange through a reduction of the extinction coefficient and deteriorates conductive heat exchange within the material through a relative increase of the fluid volume which has a lower conductivity than the solid. The effect of porosity on overall heat transfer is thus a trade-off between these two mechanisms and the changed thermal mass of the element. At high temperatures above about 1000 K, radiation heat exchange dominates the thermal energy transfer within the material. Consequently, when the porosity is increased, heat can be diffused more easily within the RPCs and an enhancement of heat exchange between the hot and cold elements is expected. The porosity of the reactive material is varied between a value of 45% and 85% in order to analyze its influence on efficiency which is shown in Fig. 6. The heat exchanger efficiency increases monotonically with porosity from a value of 19.9% at 45% porosity to 49.7% at 85% porosity. Cycle efficiency rises from 7.6% to 9.9%. This result confirms the enhancement of heat exchanger efficiency with an increase of porosity due to the reduction of the thermal mass of the elements and better radiative penetration of the element volume through a reduced extinction coefficient.

This conclusion is valid for the porosity formulation used in the calculations which relies on a mean pore diameter. For a further evolution of the porous reactive material, a gradual change of porosity with large pores for the inlet of direct irradiation and a decrease of porosity inside the volume to increase the mass loading could be beneficial. However, the description of this gradual change in porosity requires an adaptation of the current model.

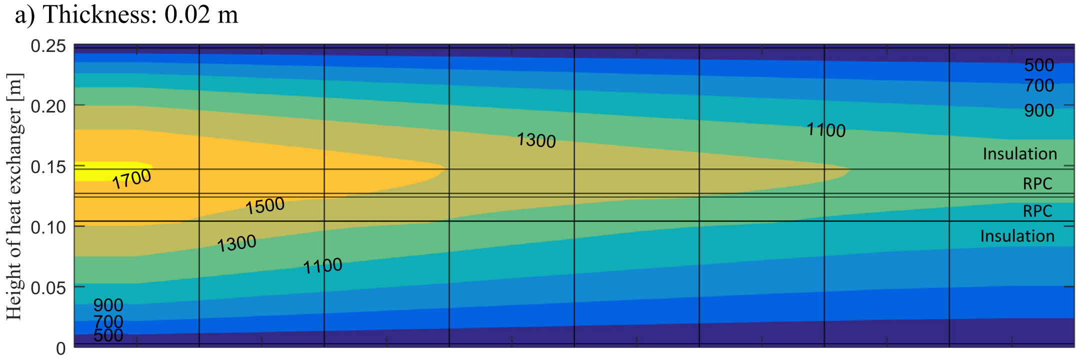
a) Thickness: 0.02 m

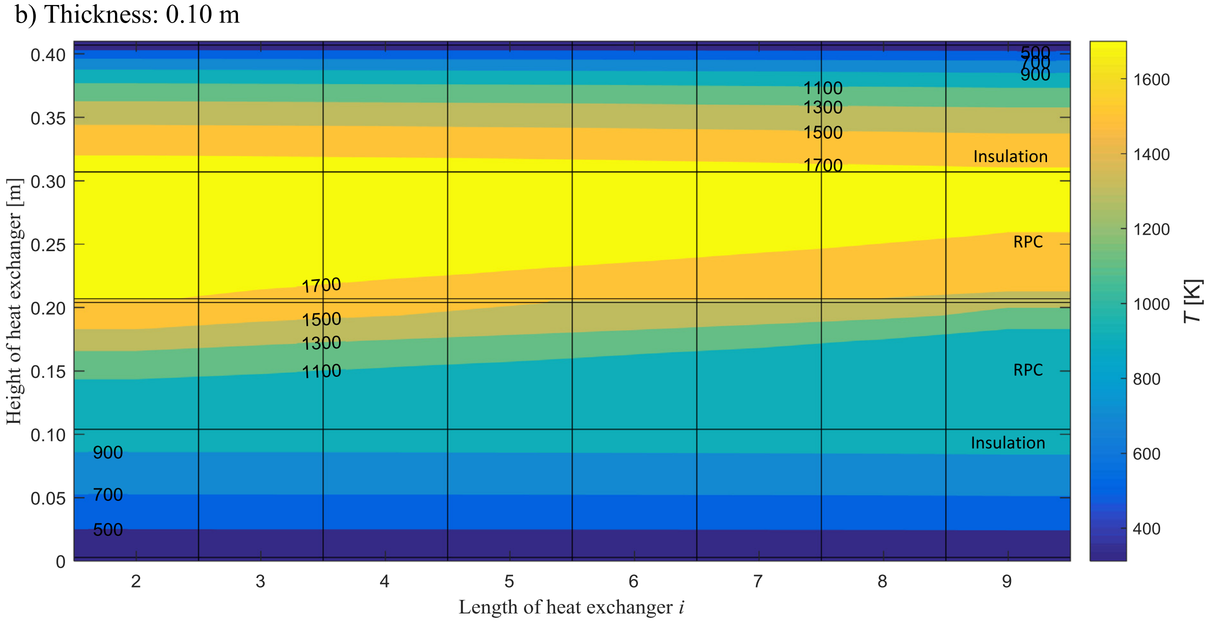
b) Thickness: 0.10 m

**Fig. 5.** Comparison of heat exchanger temperature profiles for an RPC thickness of (a) 0.02 m and (b) 0.10 m at a porosity of 80%. The heat exchanger has eight chambers $(2 \leqslant i \leqslant 9)$. Shown is the temperature profile of the heat exchanger including insulation and walls. The thinner material is heated more evenly to a higher temperature and thus allows for a higher heat exchanger efficiency (compare temperature profile in lower chamber half at $i = 2$). Parameter values are shown in Table 2.

### 4.3. Length of heat exchanger

An increased number of heat exchanger chambers at a constant chamber length, i.e. increased physical length of the heat exchanger, introduces heat exchange on more intermediate temperature levels and thus changes the characteristic towards a continuous counter-flow heat exchanger. A larger residence time, on the other hand, intensifies heat exchange in the existing number of chambers. In the following, both the number of heat exchanger chambers and the residence time of the elements per chamber, are varied to analyze their influence on efficiency. In Fig. 7, heat exchanger efficiency is shown as a function of the number of heat exchanger chambers $n_{\mathrm{he}}$ (excluding the reaction chambers, i.e. $n_{\mathrm{he}} = n - 2$ in Fig. 1) and residence time of the elements per heat exchanger chamber. The number of heat exchanger chambers is varied between zero and 20, and the residence time is varied between one second and 100 s. In general, a direct correlation between the number of chambers and the residence time is visible which means that a certain level of efficiency can be reached with a number of parameter combinations. For example, $\eta_{\mathrm{he}} = 0.4$ can be reached with $n_{\mathrm{he}} = 20$ and $\Delta t = 14s$, or $n_{\mathrm{he}} = 5$ and $\Delta t = 60s$. With interest in a compact heat exchanger, a low number of chambers can be chosen and the residence time can be adjusted accordingly.

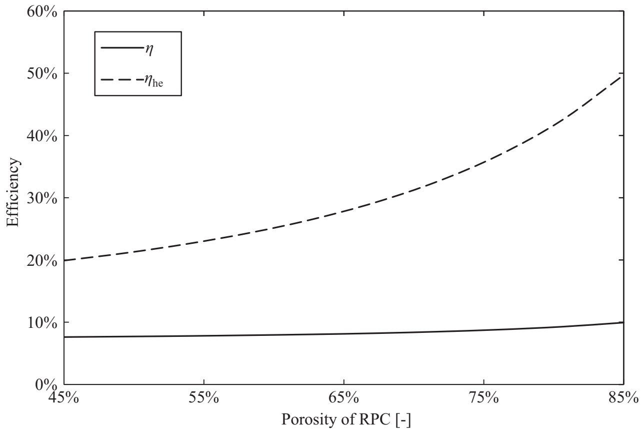

**Fig. 6.** Heat exchanger efficiency $\eta_{\mathrm{he}}$ and cycle efficiency $\eta$ as a function of porosity of the reactive elements for a heat exchanger with eight chambers, a residence time of 40 s and an element thickness of 0.05 m. Parameter values are shown in Table 2.

The largest efficiency that can be reached in the chosen parameter space is over 60% which requires a heat exchanger with at least 11 chambers at a residence time of 80 s.

In Fig. 7, both an increase in residence time and number of chambers increases efficiency, which indicates a dependency on the total residence time $n_{\mathrm{he}} \times \Delta t$ of the elements in the heat exchanger. A given total residence time can be achieved with a

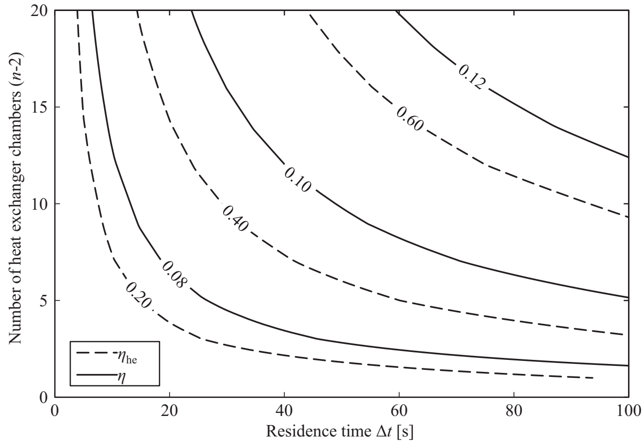

**Fig. 7.** Cycle efficiency $\eta$ and heat exchanger efficiency $\eta_{he}$ as a function of the number of heat exchanger chambers ($n-2$) and residence time per chamber $\Delta t$. All other parameter values are shown in Table 2.

combination of $n_{he}$ and $\Delta t$, however, it should be expected that there are limitations to this principle, specifically regarding the chosen number of chambers: a smaller number of chambers forces the heat exchange to take place on fewer levels of temperature, while a larger number of chambers introduces more temperature levels and thus should approach the ideal counter-flow heat exchanger more closely. The entropy change associated with the heat exchange process is proportional to the temperature difference of the chamber halves, and is thus higher for a smaller number of chambers.

In Fig. 8, heat exchanger efficiency is shown as a function of the total residence time of the elements in the heat exchanger for different heat exchanger lengths. As expected, for a given value of total residence time, efficiency increases with the number of heat exchanger chambers up to about $n_{he} = 15$. The highest heat exchanger efficiency is reached at $n_{he} \times \Delta t \approx 3000$ s for $n_{he} \geqslant 15$. At small values of $n_{he} \times \Delta t$, efficiency shows a strong increase for all $n_{he}$. If the total residence time exceeds its optimum value, efficiency decreases due to the assumed losses to the environment. With the information given about the dependency of efficiency on the number of chambers and residence time, it is possible to design the heat exchanger length to maximize efficiency.

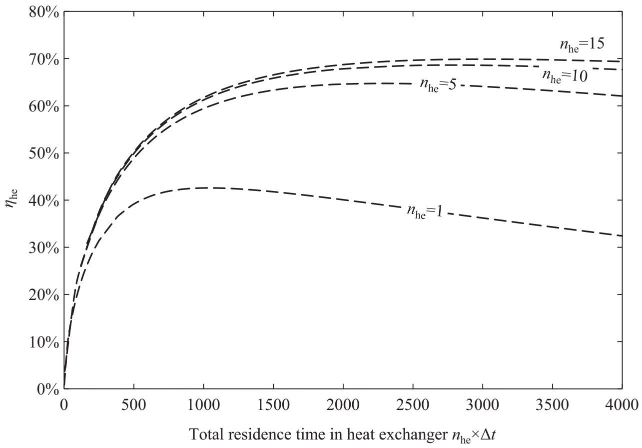

**Fig. 8.** Heat exchanger efficiency as a function of the total residence time of the elements in the heat exchanger $n_{he} \times \Delta t$. At a given value of total residence time, a larger number of chambers reduces the irreversibilities of the heat exchange process by introduction of more intermediate temperature levels.

## 5. Conclusions

A generic and modular model is presented for the description of solar thermochemical syngas production incorporating solid heat exchange in a counter-flow arrangement of the reactive material. Heat recuperation is achieved by the transfer of energy by thermal radiation between reduced and oxidized elements of reactive material through a thin separation wall having high thermal conductivity and emissivity. Heat diffusion in the porous domains of the reactive material and the insulation occurs by conduction and radiation, while convection is neglected due to its small influence. Radiation heat transfer is described with the Rosseland diffusion approximation and conduction with the three resistor model, where a validation is performed with Monte Carlo simulations.

Both external and internal heat exchange processes between the elements as well as within the elements have to be considered for heat exchanger design. For a large material thickness and low porosity, the element mass is high and internal heat diffusion can be slow compared to the residence time in the heat exchanger which leads to a challenge to dissipate the exchanged heat within the material. As only a part of the material is effectively participating in the heat exchange, this negatively influences the heat exchange process and therefore heat exchanger efficiency. A better performance can be achieved through a decrease of the material mass by reducing the thickness, an increase of the residence time, or an increase of material porosity.

An increase in material porosity (at a proportionally larger mean pore diameter) achieves a better penetration of the radiation into the material volume and at the same time decreases thermal conductivity and mass. The effects of higher volumetric radiation penetration and reduced thermal mass outweigh the reduced thermal conductivity and thus a higher porosity increases the heat exchanger efficiency.

A correlation exists between heat exchanger length and residence time, allowing different combinations of these two variables at constant heat exchanger efficiency. Within certain limits and with respect to a simpler concept, it is therefore advantageous to design the heat exchanger with a shorter length and a correspondingly longer residence time of the elements per chamber. In principle, $\eta_{he}$ close to 70% is possible with an adequate combination of length and residence time. However, the achievement of the maximum heat exchanger efficiency requires a certain number of chambers and thus physical length, as irreversibilities are reduced for a larger number of intermediate temperature levels. The efficiency of the thermodynamic cycle is derived under the assumptions of a concentration ratio of 3000, vacuum pumping, separation of the resulting $CO/CO_2$ gas mixture, radiation losses from the reduction chamber, heat recuperation from the gas phase, and an efficiency of 40% for the conversion of heat to electricity. The energy requirements for vacuum pumping, gas separation, and the energy lost by reradiation limit the cycle efficiency to values of about 12%. Higher cycle efficiencies of over 20% are possible using more favorable assumptions of decreased energy penalties and higher operating temperatures. This may require progress in the field of material design, possibly with a different redox material, to increase the reduction temperature and to reduce the reduction enthalpy or increase the nonstoichiometry.

The presented model including the description of heat diffusion within the reactive material is a valuable tool for the design of heat exchangers and helps to identify technically interesting reactor concepts for the achievement of high energy conversion efficiencies.

## Acknowledgements

The authors gratefully acknowledge the contribution of Valentin Batteiger, Arne Roth and Parthasarathy Pandi. The research

**Table 3**
Material properties used in the simulations.

| Inconel | Unit | Source |
|---|---|---|
| $\varepsilon_{\mathrm{Inc}} = 0.69$ | – | Special Metals (2015) |
| $\lambda_{\mathrm{Inc}} = 15.9$ | $\mathrm{W\,m^{-1}\,K^{-1}}$ | Special Metals (2015) |
| $c_{p,\mathrm{Inc}} = 465$ | $\mathrm{J\,kg^{-1}\,K^{-1}}$ | Special Metals (2015) |
| $\rho_{\mathrm{Inc}} = 8470$ | $\mathrm{kg\,m^{-3}}$ | Special Metals (2015) |
| *Ceria $CeO_2$* | | |
| $c_{p,\mathrm{CeO_2}} = (67.95 - 9.9 \times 10^5 \cdot T^{-2} + 0.01 \cdot T)/M_{\mathrm{CeO_2}}$ | $\mathrm{J\,kg^{-1}\,K^{-1}}$ | Riess et al. (1986) |
| $\lambda_{\mathrm{CeO_2}} = 4.61 \cdot \left(\frac{T}{1000}\right)^4 - 26.64 \cdot \left(\frac{T}{1000}\right)^3 + 58.30 \cdot \left(\frac{T}{1000}\right)^2 - 59.28 \cdot \left(\frac{T}{1000}\right) + 25.52$ | $\mathrm{W\,m^{-1}\,K^{-1}}$ | Touloukian et al. (1971) |
| $\varepsilon_{\mathrm{CeO_2}} = 0.5 + \frac{T-1100}{(1300-1100)} \cdot 0.4$; $1100\ \mathrm{K} < T < 1300\ \mathrm{K}$ | – | Touloukian and DeWitt (1972) |
| *Ceria-RPC* | | |
| $\beta_{\mathrm{RPC}} = 1.765 \cdot \sqrt{1-\varphi}/(2.2 \times 10^{-3} \cdot \varphi + 7.59 \times 10^{-4})$ | $\mathrm{m^{-1}}$ | Suter et al. (2014) |
| $\lambda_{\mathrm{RPC}} = \lambda_{\mathrm{CeO_2}} \cdot \left[\left(1 - \sqrt{g_0 - g_1 \varepsilon_{\mathrm{CeO_2}}}\right) \frac{\lambda_{O_2}}{\lambda_{\mathrm{CeO_2}}} \cdot \left(\varepsilon_{\mathrm{CeO_2}} + (1 - \varepsilon_{\mathrm{CeO_2}}) \frac{\lambda_{O_2}}{\lambda_{\mathrm{CeO_2}}}\right) + \sqrt{g_0 - g_1 \varepsilon_{\mathrm{CeO_2}}} \left(\varepsilon_{\mathrm{CeO_2}} \frac{\lambda_{O_2}}{\lambda_{\mathrm{CeO_2}}} + (1 - \varepsilon_{\mathrm{CeO_2}})\right)\right]$ | $\mathrm{W\,m^{-1}\,K^{-1}}$ | Suter et al. (2014) |
| $g_0 = 0.754$; $g_1 = 0.829$ | | |
| $\rho_{\mathrm{RPC}} = \rho_{\mathrm{CeO_2}} \cdot (1 - \varphi)$ | $\mathrm{kg\,m^{-3}}$ | |
| *Separating wall made from $SiC_{0.75}/HfC_{0.25}$* | | |
| $\varepsilon_{\mathrm{SiC/HfC}} = 0.85$ | – | Ultramet (2015) |
| $\lambda_{\mathrm{SiC/HfC}} = 80$ | $\mathrm{W\,m^{-1}\,K^{-1}}$ | Desmaison-Brut et al. (2007) |
| $c_{p,\mathrm{SiC/HfC}} = 0.75 \cdot 670 + 0.25 \cdot 200$ | $\mathrm{J\,kg^{-1}\,K^{-1}}$ | Ultramet (2015) |
| $\rho_{\mathrm{SiC/HfC}} = 0.75 \cdot 3210 + 0.25 \cdot 12700$ | $\mathrm{kg\,m^{-3}}$ | Ultramet (2015) |
| *Separating wall made from solid $Al_2O_3$* | | |
| $\lambda_{\mathrm{Al_2O_3}} = 35$ | $\mathrm{W\,m^{-1}\,K^{-1}}$ | Accuratus (2016) |
| $c_{p,\mathrm{Al_2O_3}} = 880$ | $\mathrm{J\,kg^{-1}\,K^{-1}}$ | Accuratus (2016) |
| $\rho_{\mathrm{Al_2O_3}} = 3890$ | $\mathrm{kg\,m^{-3}}$ | Accuratus (2016) |
| *$Al_2O_3$-insulation* | | |
| $\lambda_{\mathrm{Ins}} = 6 \times 10^{-8} T^2 - 2 \times 10^{-5} T + 0.08 + \frac{16\sigma T^3}{3\beta_{\mathrm{Ins}}}$ | $\mathrm{W\,m^{-1}\,K^{-1}}$ | Zircar Zirconia (2015) |
| $\beta_{\mathrm{Ins}} = 1.73 \times 10^{-8} T^4 - 5.00 \times 10^{-5} T^3 + 6.13 \times 10^{-2} T^2 - 31.53T + 1.08 \times 10^4$ | $\mathrm{m^{-1}}$ | Zhang et al. (2007) |
| $c_{p,\mathrm{Ins}} = 4 \times 10^{-7} \cdot T^3 - 1.38 \times 10^{-3} \cdot T^2 + 1.60 \cdot T + 477.70$ | $\mathrm{J\,kg^{-1}\,K^{-1}}$ | Furler (2014) |
| *Gases* | | |
| $\lambda_{O_2} = -1.29 \times 10^{-3} + 0.11 \times 10^{-3} \cdot T - 0.05 \times 10^{-6} \cdot T^2 + 0.03 \times 10^{-9} \cdot T^3 - 0.01 \times 10^{-12} \cdot T^4$ | $\mathrm{W\,m^{-1}\,K^{-1}}$ | Kleiber and Joh (2013) |
| $c_{p,\mathrm{CO}} = -30.1 \cdot \left(\frac{T}{1000}\right)^5 + 250.8 \cdot \left(\frac{T}{1000}\right)^4 - 770.9 \cdot \left(\frac{T}{1000}\right)^3 + 1008.9 \cdot \left(\frac{T}{1000}\right)^2 - 349.2 \cdot \left(\frac{T}{1000}\right) + 1072.8$ | $\mathrm{J\,kg^{-1}\,K^{-1}}$ | Engineering Toolbox (2015) |
| $c_{p,\mathrm{CO_2}} = 14.2 \cdot \left(\frac{T}{1000}\right)^5 - 146.6 \cdot \left(\frac{T}{1000}\right)^4 + 615.6 \cdot \left(\frac{T}{1000}\right)^3 - 1353.5 \cdot \left(\frac{T}{1000}\right)^2 + 1646.2 \cdot \left(\frac{T}{1000}\right) + 458.5$ | $\mathrm{J\,kg^{-1}\,K^{-1}}$ | Engineering Toolbox (2015) |
| $M_{\mathrm{CeO_2}} = 0.172$ | $\mathrm{kg\,mol^{-1}}$ | Lapp (2013) |

leading to these results has received funding from the European Union's Horizon 2020 research and innovation programme under grant agreement no. 654408.

## Appendix A

See Table 3.

## References

Accuratus, 2016. Aluminum Oxide, Al2O3 Ceramic Properties [WWW Document]. URL <http://accuratus.com/alumox.html> (accessed 3.25.16).

Chueh, W.C., Falter, C., Abbott, M., Scipio, D., Furler, P., Haile, S.M., Steinfeld, A., 2010. High-flux solar-driven thermochemical dissociation of $CO_2$ and $H_2O$ using nonstoichiometric ceria. Science 330, 1797–1801. http://dx.doi.org/10.1126/science.1197834.

Chueh, W.C., Haile, S.M., 2010. A thermochemical study of ceria: exploiting an old material for new modes of energy conversion and $CO_2$ mitigation. Philos. Trans. A Math. Phys. Eng. Sci. 368, 3269–3294. http://dx.doi.org/10.1098/rsta.2010.0114.

Desmaison-Brut, M., Tétard, D., Tixier, C., Faure, C., Chabas, E., 2007. Mechanical Properties and Oxidation Behaviour of Electroconductive Ceramic Composites. In: 10th Int. Conf. Eur. Ceram. Soc., pp. 1315–1320.

Diver, R.B., Miller, J.E., Allendorf, M.D., Siegel, N.P., Hogan, R.E., 2008. Solar thermochemical water-splitting ferrite-cycle heat engines. J. Sol. Energy Eng. 130, 041001. http://dx.doi.org/10.1115/1.2969781.

Engineering Toolbox, 2015. Specific Heat Capacity of Gases [WWW Document]. URL <www.engineeringtoolbox.com> (accessed 10.30.15).

Ermanoski, I., Siegel, N.P., Stechel, E.B., 2013. A new reactor concept for efficient solar-thermochemical fuel production. J. Sol. Energy Eng. 135, 031002. http://dx.doi.org/10.1115/1.4023356.

Falter, C., Batteiger, V., Sizmann, A., 2016. Climate impact and economic feasibility of solar thermochemical jet fuel production. Environ. Sci. Technol. 50, 470–477. http://dx.doi.org/10.1021/acs.est.5b03515.

Falter, C.P., Sizmann, A., Pitz-Paal, R., 2015. Modular reactor model for the solar thermochemical production of syngas incorporating counter-flow solid heat exchange. Solar Energy 122, 1296–1308. http://dx.doi.org/10.1016/j.solener.2015.10.042.

Felinks, J., 2014. Private communication.

Felinks, J., Brendelberger, S., Roeb, M., Sattler, C., Pitz-paal, R., 2014. Heat recovery concept for thermochemical processes using a solid heat transfer medium. Appl. Thermal Eng. 73, 1004–1011. http://dx.doi.org/10.1016/j.applthermaleng.2014.08.036.

Furler, P., 2014. Solar thermochemical $CO_2$ and $H_2O$ splitting via ceria redox reactions. Dissertation, ETH Zürich. doi:http://dx.doi.org/10.3929/ethz-a-010207593.

Furler, P., Scheffe, J., Gorbar, M., Moes, L., Vogt, U., Steinfeld, A., 2012a. Solar thermochemical $CO_2$ splitting utilizing a reticulated porous ceria redox system. Energy Fuels 26, 7051–7059. http://dx.doi.org/10.1021/ef3013757.

Furler, P., Scheffe, J., Marxer, D., Gorbar, M., Bonk, A., Vogt, U., Steinfeld, A., 2014. Thermochemical $CO_2$ splitting via redox cycling of ceria reticulated foam structures with dual-scale porosities. Phys. Chem. Chem. Phys.: PCCP 16, 10503–10511. http://dx.doi.org/10.1039/c4cp01172d.

Furler, P., Scheffe, J.R., Steinfeld, A., 2012b. Syngas production by simultaneous splitting of $H_2O$ and $CO_2$ via ceria redox reactions in a high-temperature solar reactor. Energy Environ. Sci. 5, 6098. http://dx.doi.org/10.1039/c1ee02620h.

Hischier, I., Hess, D., Lipiński, W., Modest, M., Steinfeld, A., 2009. Heat transfer analysis of a novel pressurized air receiver for concentrated solar power via combined cycles. J. Therm. Sci. Eng. Appl. 1, 041002. http://dx.doi.org/10.1115/1.4001259.

Howell, J.R., Siegel, R., Mengüc, M., Pinar, R., 2011. Thermal Radiation Heat Transfer. CRC Press, Boca Raton.

International Energy Agency, 2016. Tracking Clean Energy Progress 2016.

Kleiber, M., Joh, R., 2013. VDI-Wärmeatlas, Kapitel D. doi:http://dx.doi.org/10.1007/978-3-642-19981-3.

Lapp, J., 2013. Thermal modeling and design of a solar non-stoichiometric redox reactor with heat recovery Dissertation. University of Minnesota.

Lapp, J., Davidson, J.H., Lipiński, W., 2013. Heat transfer analysis of a solid-solid heat recuperation system for solar-driven nonstoichiometric cycles. J. Sol. Energy Eng. 135, 031004. http://dx.doi.org/10.1115/1.4023357.

Lapp, J., Davidson, J.H., Lipiński, W., 2012. Efficiency of two-step solar thermochemical non-stoichiometric redox cycles withheat recovery. Energy 37, 591–600. http://dx.doi.org/10.1016/j.energy.2011.10.045.

Loretz, M., Maire, E., Baillis, D., 2008. Analytical modelling of the radiative properties of metallic foams: contribution of X-ray tomography. Adv. Eng. Mater. 10, 352–360. http://dx.doi.org/10.1002/adem.200700334.

Marxer, D.A., Furler, P., Scheffe, J.R., Geerlings, H., Falter, C., Batteiger, V., Sizmann, A., Steinfeld, A., 2015. Demonstration of the entire production chain to renewable kerosene via solar-thermochemical splitting of $H_2O$ and $CO_2$. Energy Fuels 29, 3241–3250. http://dx.doi.org/10.1021/acs.energyfuels.5b00351.

Panlener, R.J., Blumenthal, R.N., Garnier, J.E., 1975. A thermodynamic study of nonstoichiometric cerium dioxide. J. Phys. Chem. Solids 36, 1213–1222. http://dx.doi.org/10.1016/0022-3697(75)90192-4.

Pfeiffer Vacuum, 2014. Private communication.

Riess, I., Ricken, M., Noelting, J., 1986. Specific heat of non-stoichiometric ceria ($CeO_y$). Solid State Ionics 18–19, 725–726. http://dx.doi.org/10.1016/0167-2738(86)90250-X.

Special Metals, 2015. Inconel Alloy 600 [WWW Document]. URL <www.specialmetals.com/documents/Inconelalloy600.pdf> (accessed 6.1.15).

Steinfeld, A., Epstein, M., 2001. Light years ahead. Chem. Britain 37, 30–32. http://dx.doi.org/10.3929/ethz-a-004274060.

Suter, S., Steinfeld, A., Haussener, S., 2014. Pore-level engineering of macroporous media for increased performance of solar-driven thermochemical fuel processing. Int. J. Heat Mass Transfer 78, 688–698. http://dx.doi.org/10.1016/j.ijheatmasstransfer.2014.07.020.

Touloukian, Y.S., DeWitt, D.P., 1972. Thermophysical Properties of Matter - The TPRC Data Series, vol. 8. Thermal Radiative Properties - Nonmetallic Solids. CINDAS/Purdue University.

Touloukian, Y.S., Powell, R.W., Ho, C.Y., Klemens, P.G., 1971. Thermophysical Properties of Matter - The TPRC Data Series, vol. 2. Thermal Conductivity - Nonmetallic Solids. CINDAS/Purdue University.

Ultramet, 2015. Ceramic Protective Coatings [WWW Document]. URL <http://www.ultramet.com/ceramic_protective_coatings.html#layered> (accessed 11.15.15).

Zeman, F., 2007. Energy and material balance of $CO_2$ capture from ambient air. Environ. Sci. Technol. 41, 7558–7563. http://dx.doi.org/10.1021/es070874m.

Zhang, B., Zhao, S., He, X., Du, S., 2007. High temperature thermal physical properties of high-alumina fibrous insulation. J. Mater. Sci. Technol. 23, 860–864.

Zircar Zirconia, 2015. Fibrous Insulation - Type Buster M35 [WWW Document]. URL <http://www.zircarzirconia.com/product-literature/buster.php> (accessed 1.1.15).